SEMARAK ILMU PUBLISHING

Semarak Engineering Journal

Journal homepage:
https://semarakilmu.my/index.php/sej/index
ISSN: 3036-0145

Advanced Damage Modelling of Primary AA6061 Aluminium Alloy Using Generalized Incremental Stress State-Dependent Damage Model (GISSMO)

Nor Aziera Azman[1,2], Liyana Syahirah Ramlan[1,2,3], Mohd Khir Mohd Nor[1,2,*], Mohd Syazwan Abdul Samad[4], Irfan Alias Farhan Latif[1,2]

[1] Crashworthiness and Collisions Research Group (COLORED), Faculty of Mechanical and Manufacturing Engineering, Universiti Tun Hussein Onn Malaysia, Parit Raja, Johor, Malaysia

[2] Advanced Materials and Manufacturing Centre (AMMC), Institute for Integrated Engineering (I2E), Universiti Tun Hussein Onn Malaysia, Parit Raja, Johor, Malaysia

[3] Structural Department, Subsea 7 Asia Pacific Sdn Bhd, Malaysia

[4] Material Engineering, Computer Aided Engineering, Ceer Motors, Saudi Arabia

ARTICLE INFO

Article history:
Received 9 March 2026
Received in revised form 27 March 2026
Accepted 28 March 2026
Available online 14 April 2026

Keywords:

Recycled Aluminium Alloy AA6061; GISSMO Fracture Mode Characterization; Uniaxial Tensile Test; Finite Element Analysis (FEA)

ABSTRACT

Aluminium alloy AA6061 is widely used in lightweight automotive structures due to its high strength-to-weight ratio. Accurate prediction of its deformation and fracture behaviour is critical for crashworthiness design. Therefore, this research establishes a high-fidelity fracture prediction framework for AA6061 primary aluminium alloy by implementing and validating the Generalized Incremental Stress-State Dependent Damage Model (GISSMO). To capture the complex transition between shear and tensile failure modes, five distinct specimen geometries which are smooth tensile, notched tensile, shear 0°, shear 45°, and large tensile that were subjected to uniaxial tensile testing across a broad spectrum of stress triaxialities. The resulting experimental data were utilized to calibrate the non-linear damage evolution and failure strain parameters within the GISSMO framework. Numerical validation was conducted via Finite Element Analysis (FEA) in Altair HyperWorks, where a rigorous comparison of force-displacement response demonstrated a high degree of correlation between the experimental and simulated curves. The comparison of simulation uniaxial tensile test force-displacement curve with experimental curve showed close agreement especially at the elastic and yield regions. Notably, the model successfully predicted the exact spatial location of fracture initiation, matching the physical rupture patterns observed in the laboratory. To ensure the integrity of the damage calibration, plasticity-only simulations were executed to isolate the material's constitutive response from damage-induced softening of Simplified Johnson-Cook model. Detailed analysis of stress and strain time histories further elucidated the localized deformation gradients within the gauge area, confirming the model's ability to track damage accumulation under heterogeneous stress states. These findings provide a robust, validated numerical tool for predicting the structural limits of AA6061, offering significant utility for high-precision engineering applications in the automotive and aerospace sectors.

* *Corresponding author.*
E-mail address: khir@uthm.edu.my

https://doi.org/10.37934/sej.13.1.208233

1. Introduction

The increasing demand of advanced lightweight materials such as aluminium alloy has led to an evolution in manufacturing methods for components and parts in the automotive industry [1-3]. Aluminium alloy AA6061, a precipitation hardened Al-Mg-Si alloy that offers a favourable balance in strength, ductility, corrosion resistance and manufacturability makes it suitable for crash-critical parts such as bumper beam and crash boxes [4-7]. However, its effective implementation in crashworthiness design requires an in-depth understanding of its deformation and fracture behaviour under various loading conditions [8-11]. Vehicle crash events involve complex stress states, and failure prediction must account for these variations to ensure structural integrity and occupant safety. To achieve a reliable structural performance in crash events, accurate prediction of deformation and fracture behaviour of the material is essential [12-20]. An accurate prediction of material and fracture behaviour requires capable damage model to capture the stress-state dependent failure across a wide range of loading conditions.

Advanced finite element simulations play a vital role in the design and optimization of such components, where ductile damage models are used to predict failure mechanisms under various loading conditions [21-22]. Among the commonly used models, the Generalized Incremental Stress State-dependent damage Model (GISSMO) has gained prominence due to its ability to incorporate stress triaxiality dependence, strain-rate sensitivity, and post-necking behaviour using a relatively simple experimental calibration approach [23]. GISSMO is especially valued in industrial applications for its compatibility with commercial solvers like LS-DYNA and HyperWorks, and for providing robust predictions using data from standard uniaxial tensile tests [24]. Unlike the standard Johnson-Cook fracture model, GISSMO allows for non-linear damage accumulation, which was found essential in capturing the abrupt failure observed in the shear specimens. The accuracy of GISSMO, however, relies heavily on comprehensive experimental data that span a range of triaxialities representative of real crash scenarios. Conventional tensile data alone are inadequate because they represent only moderate triaxial tension, failing to capture behaviour under high-constrain or shear-dominated conditions [25-30]. Therefore, the selection of appropriate specimen geometries is crucial to fully characterize the stress-state dependency of ductile fracture in AA6061.

Specimen geometry has a significant influence on mechanical response, stress distribution, and the onset of localisation [31]. Smooth tensile specimens typically provide material properties such as elastic modulus, yield stress, and ultimate tensile strength under uniform stress distribution. Large tensile specimens help to assess size effects and deformation stability, whereas notched specimens induce high stress triaxiality, accelerating void nucleation and growth [32]. Shear specimens, including 0° and 45° configurations, subject the material to low-triaxiality stress states dominated by shear localisation [33]. Previous studies have highlighted that AA6061 exhibits marked sensitivity to stress triaxiality, where fracture strain decreases with increasing constraint and varies significantly under shear-dominated loading [34-36]. Despite these findings, most existing research focuses on either tensile or notched conditions in isolation, with limited studies incorporating shear specimens or combining all three stress states into a unified characterization framework.

The lack of integrated datasets that incorporate smooth tensile, large tensile, notched tensile, and shear specimens limits the ability of numerical models to fully represent the fracture envelope of AA6061. Moreover, existing studies often do not address the effects of specimen geometry on key mechanical properties, nor do they provide detailed comparisons across different stress states. These gaps hinder the application of AA6061 in advanced crashworthiness simulations, where precise prediction of material failure is critical.

To address these limitations, the present study investigates the deformation and fracture behaviour of primary AA6061 using five specimen geometries selected to represent a broad range of triaxialities relevant to automotive crash loading. This includes the influence of smooth, notched and shear geometries into a unified GISSMO calibration framework. Through comprehensive uniaxial tensile experiments and GISSMO calibration, this work provides a complete dataset tailored for damage model development. The resulting model enhances the predictive capability of finite element simulations and contributes to ongoing efforts in designing safer and lighter automotive structures.

2. Characterization of GISSMO Damage Model

This section describes the characterization process of the GISSMO damage model, starting with the experimental characterization by using multiple specimen geometries, extraction of fracture plastic strain from true stress- true strain curves from the experimental results, determination of stress triaxiality via finite element method and validation of characterized GISSMO damage model through one-to-one comparison of experimental and numerical responses. These workflows are crucial in calibration of GISSMO damage model to ensure a reliable damage model is generated.

To accurately characterize the GISSMO damage model, five specimens with distinct geometries were carefully designed, as illustrated in Figure 1. These specimens of small tensile, notched tensile, shear 0°, shear 45°, and large tensile were chosen to represent a broad spectrum of stress states, ranging from predominantly shear-dominated conditions ($\eta \approx 0$) to high-triaxial tensile states ($\eta \approx 1$). By capturing this wide range of stress triaxiality, the experimental data provide a robust foundation for calibrating the fracture model, ensuring it can reliably predict ductile fracture behaviour under various loading conditions and geometrical constraints.

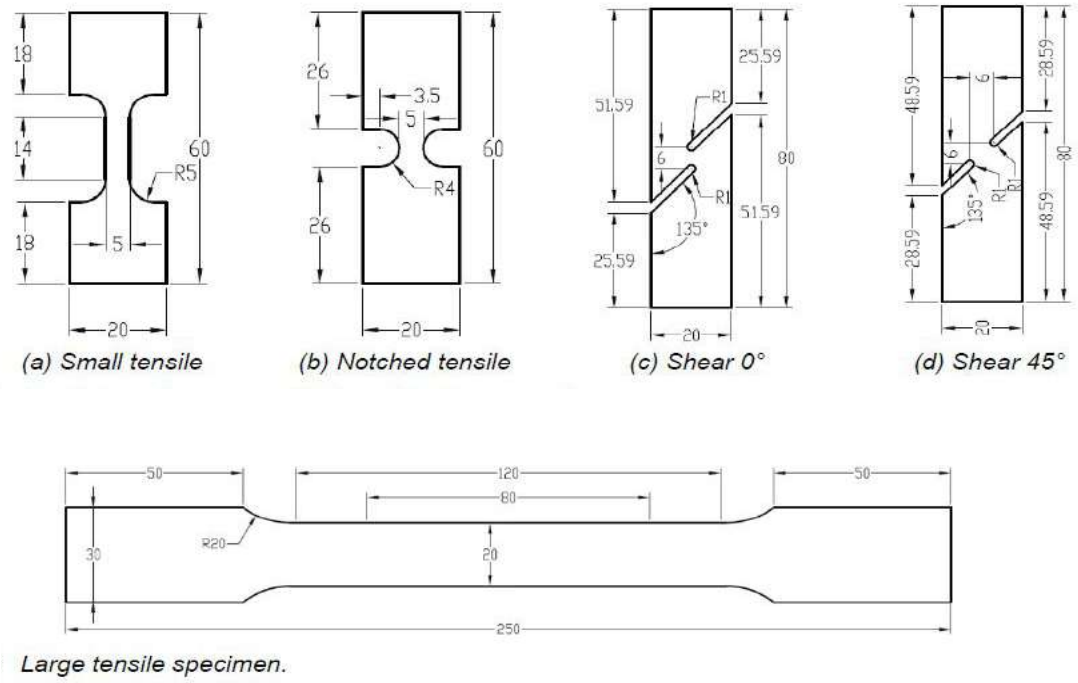

Fig. 1. Test Specimens for Complete Characterization and Derivation of Material Constants

Furthermore, Figure 2 shows the produced specimens that undergo uniaxial tensile test with thickness of 1mm. The uniaxial tensile tests were performed using a universal testing machine (Zwick Roell Z030), equipped with a high-precision extensometer to guarantee accurate measurement of axial strain throughout the loading process, as depicted in Figure 3. The detailed experimental setup, including extensometer positioning and specimen alignment within the machine, is shown in Figure 4. The uniaxial tensile test specifications were summarized in Table 1. This careful setup ensured precise and consistent data acquisition, particularly in the critical regions of necking and fracture, where localized deformation dominates, and accurate strain measurement is essential for GISSMO calibration. The results from the uniaxial tensile tests were plotted as force–displacement curves, as shown in Figure 5.

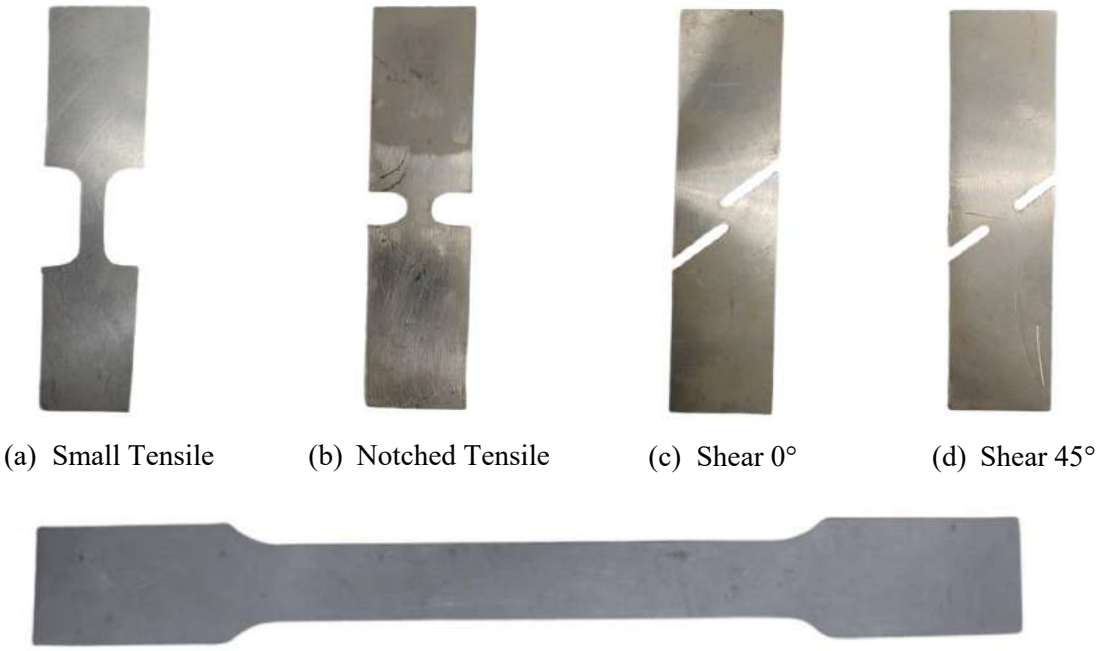

Fig. 2. Produced Test Specimens of Aluminium Alloy AA6061

Fig. 3. Zwick Roell Z030 Universal Tensile Testing Machine 10KN

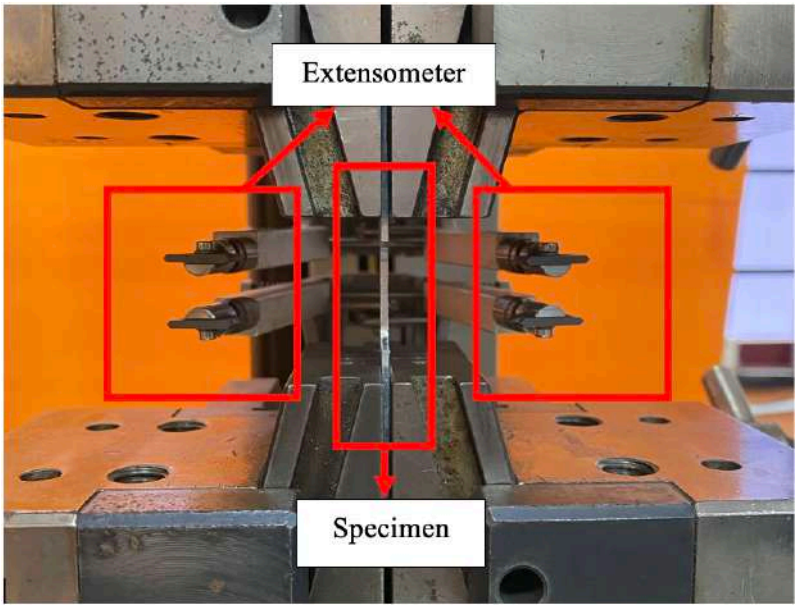

Fig. 4. Uniaxial Tensile Test Configuration

Table 1
Uniaxial Tensile Test Specifications

Specifications	Value
Strain Rate	0.001/s
Temperature	Room temperature (23℃ – 26℃)

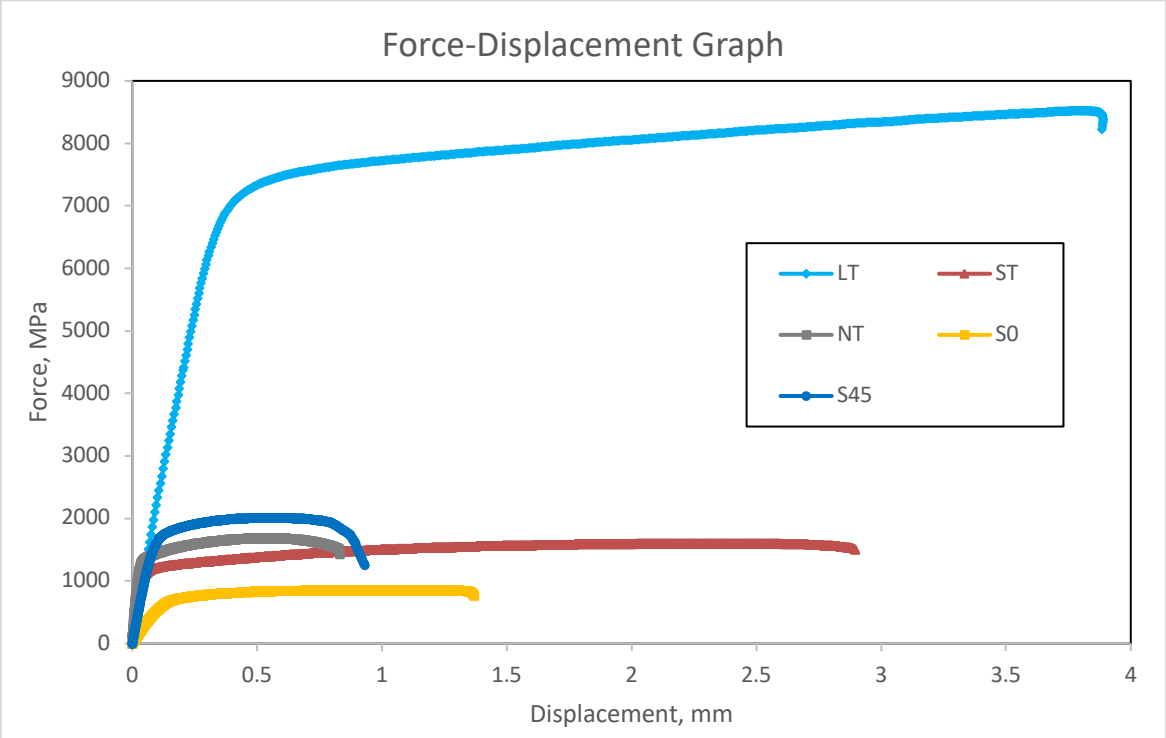

Fig. 5. Force-Displacement Graph of Each Specimen

2.1 Mechanical Properties Characterization

From the uniaxial tensile test, the force-displacement curves were plotted. These curves were converted to engineering stress-strain curve to analyse the mechanical properties of each specimen in terms of Young Modulus, E, Yield stress, σ_Y, Ultimate tensile strength (UTS) and fracture strain. Figure 5 shows the engineering stress-strain curve for each type of specimen. Table 2-6 summarize the mechanical properties for all the specimens.

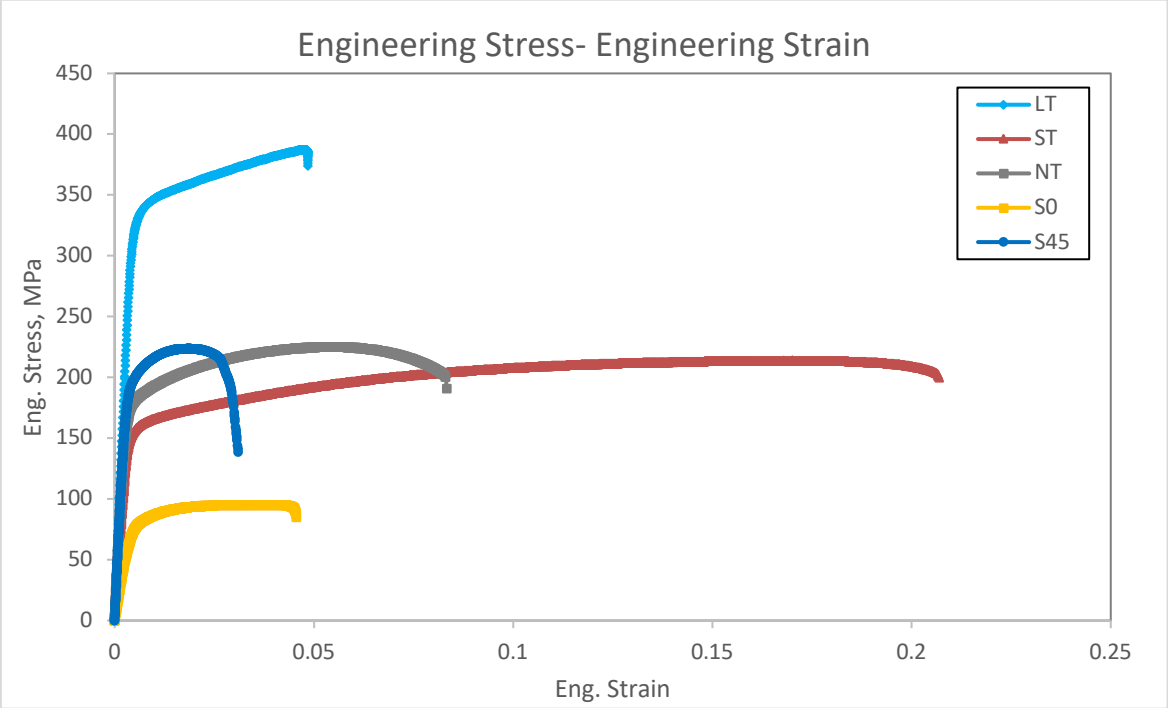

Fig. 6. Engineering Stress-Engineering Strain Graph

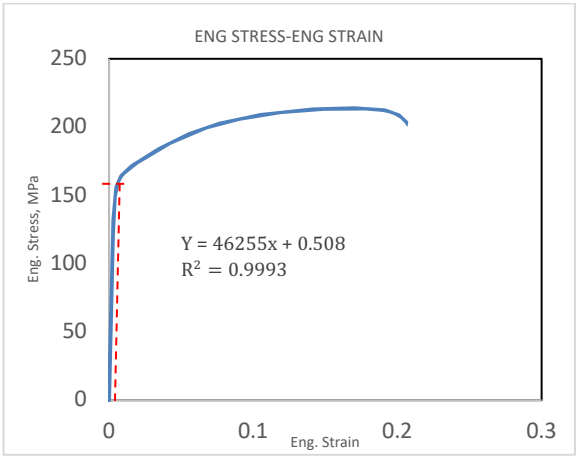

(a) Small Tensile

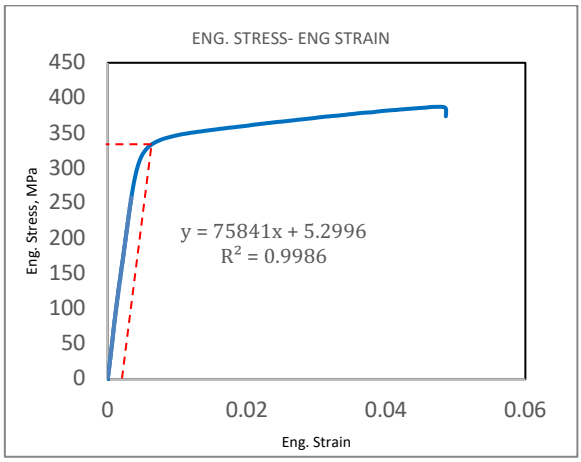

(b) Large Tensile

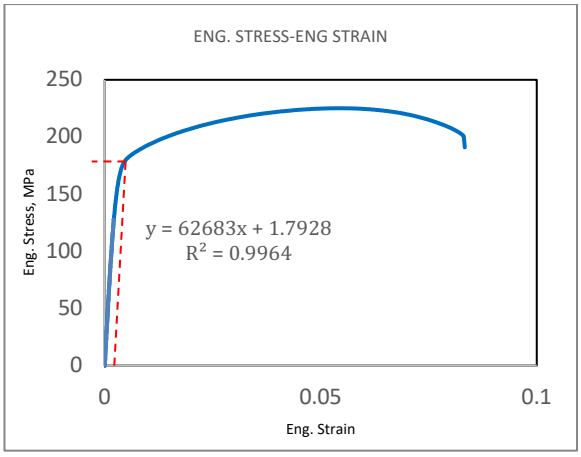

(c) Notched Tensile

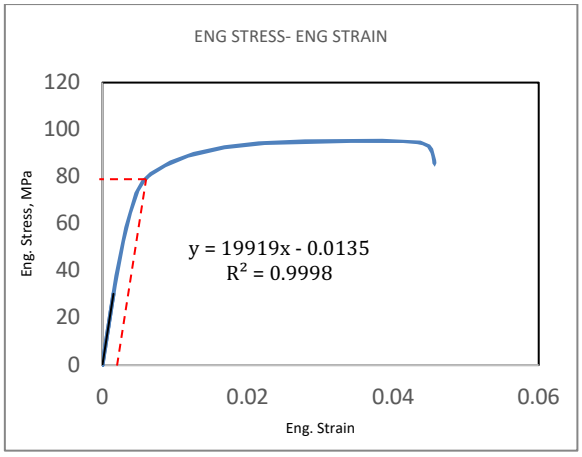

(d) Shear 0°

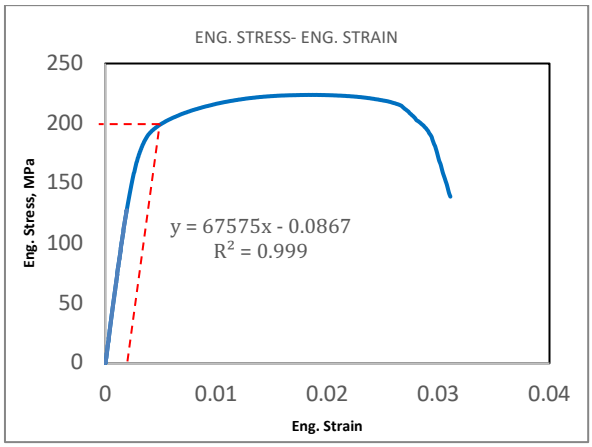

(e) Shear 45°

Fig. 7. Engineering Stress-Strain Curves of each Specimen; (a) Small Tensile; (b) Large Tensile; (c) Notched Tensile; (d) Shear 0°; (e) Shear 45°

Table 2
Mechanical Properties of Each Specimen

Type of specimens	Young Modulus, E (MPa)	Yield Stress, σ_Y (MPa)	Ultimate Tensile Strength, (UTS) (MPa)	Fracture Strain	Total Elongation (mm)
Small Tensile	46255	152.64	213.80	0.207	2.898
Large Tensile	75841	329.34	387.43	0.05	3.886
Notched Tensile	62683	176.76	225.14	0.083	0.833
Shear 0°	19919	77.64	95.29	0.046	1.370
Shear 45°	67575	198.67	223.82	0.031	0.932

The listed mechanical properties show significant variation across different specimen geometries. These differences arise primarily from the change in stress state, strain distribution and localised deformation behaviour that were altered by the geometry of specimens. For tensile specimens, the Young's modulus of

small tensile (46255MPa) was recorded to be slightly lower compared to large tensile (75841MPa). This observed difference may be influenced by the higher machine compliance sensitivity in smaller specimens which known as measurement artefact. This observation was supported by studies of Mishra et al., and Harwell et al. which stated that the differences in elastic slope and strength can arise from fixture compliance, gauge length and specimen size rather than true changes in material stiffness [37-38]. Next, the larger tensile specimen has higher value of yield stress and UTS compared to small tensile specimen. This occurred as larger specimen have more uniform stress distribution and experience less premature necking compared to small tensile which promotes early localisation that reduce the ability of material hardening before reaching maximum load.

Furthermore, notched tensile specimen exhibits intermediate mechanical properties as this behaviour is controlled by notch radius. The notch radius increases the stress concentration (local stress) at the neck section that cause the specimen to yielding earlier at the notch region. However, due to the geometric constraint the specimen can slightly withstand higher load before fracture leading to increasing in strength values. The increased constraint around the notch led to increases in stress triaxiality which promotes earlier void nucleation and faster crack propagation that reduce the material ductility. These observations were supported by the studies of Ding et al. and Hong et al., which shows the notched and constrained tensile specimens increase the local stress triaxiality and reduce the fracture strain [39-40].

Moreover, shear specimens portray the lowest strength and ductility among all specimens as it was design to generate low stress triaxiality condition where deformation of specimen is dominated by shearing rather than stretching and the material yield earlier under shear loading. The shear 45° specimen shows higher strength compared to shear 0° as it is influences by mixed loading mode (shear and tension) and have larger effective load-bearing area under diagonal loading. This observation is supported by studies of Ding et al. and Hong et al., as it reported that shear-type tensile shows little void growth, experience early shear fracture and poor agreement with void models [39-40]. This explained the low yield, UTS and low fracture strain value of shear specimens compared to other specimens.

2.2 Data Analysis for GISSMO Damage Model Parameters

As reported in the previous study by Azman et al., the accurate determination of GISSMO damage model parameters relies on both fracture plastic strain and stress triaxiality data. These critical data were derived from the uniaxial tensile tests by analysing the force-displacement curves of each specimen and applying standard conversion formulas, as presented in Equations 1 and 2. Using these equations, the raw load and displacement measurements shown in Figure 6 were converted into stress and strain values by accounting for the specimen's initial cross-sectional area and gauge length. Integration of the force-displacement data produced the engineering stress-strain curves, which serve as the foundational baseline. These curves were then further transformed into true stress-strain representations, which it is a necessary step for precise extraction of GISSMO parameters and reliable calibration of the fracture model.

$$\sigma_{Eng.} = \frac{F}{A} \quad \text{(Equation 1)}$$

$$\varepsilon_{Eng.} = \frac{Displacement}{Gauge\ Length} \quad \text{(Equation 2)}$$

where $\sigma_{Eng.}$, F, A and $\varepsilon_{Eng.}$ are engineering stress, force, area and engineering strain, respectively. From the plotted force–displacement curves in Figure 5, the corresponding true stress–true strain relationships were derived for each specimen geometry by using Equations 3 and 4. The σ_{True} represents the true stress value and the ε_{true} represents the value of true strain for the experiment. The point of fracture was clearly identified for all specimens based on the final data point recorded before failure.

$$\sigma_{true} = \left[\sigma_{Eng} \times \left(1 + \varepsilon_{Eng.}\right)\right] \quad \text{(Equation 3)}$$

$$\varepsilon_{true} = \left[ln\left(1 + \varepsilon_{Eng.}\right)\right] \quad \text{(Equation 4)}$$

The fracture strains for smooth, notched, and shear specimens derived via Equation 4 are considered formally valid. Although this analytical approach is typically reserved for smooth specimens under uniform deformation, the primary aluminium AA6061 alloy exhibits negligible post-necking deformation, with fracture occurring almost immediately following the onset of localization. This behaviour results in a minimal necking zone across all geometries. Consequently, the reduction in cross-sectional area at the fracture plane remains marginal, allowing Equation 4 to provide a sufficiently accurate approximation of fracture strain. This is empirically supported by Figure 8, which illustrates that the small tensile specimens exhibited no discernible necking within the gauge area prior to failure. Therefore, the application of standard conversion formulas (Equations 1–4) to extract true stress-strain data is justified, forming a critical component of the calibration workflow for the GISSMO damage model.

Fig. 8. Deformed Specimen after Uniaxial Tensile Test

Similar approaches have been reported in the literature for materials with negligible post-necking life, where uniform-strain formulations remain applicable up to fracture. As reported by Latif et al. [41], the recycled AA6061 alloy exhibits a mild-ductile behaviour with a very limited post-necking life, primarily due to microstructural degradation introduced during the recycling process. Consequently, fracture occurs shortly after the onset of local necking, and the deformation remains nearly uniform up to that point. Under these conditions, the assumptions underlying Equations 1 to 4 namely uniform strain distribution before necking remain valid because the contribution of strain localisation to the overall deformation is minimal.

The negligible post-necking ductility observed in this study aligns with the findings of Hyun et al. (2014) [42], who demonstrated that materials with limited deformation post-localization can be accurately characterized using pre-necking strain conversion formulations without introducing significant analytical error. This methodology is consistent with established computational workflows for 6000-series aluminum alloys. Specifically, the application of engineering-to-true stress-strain conversions during the pre-necking phase—as utilized by Koch et al. [43] and Chen et al. [44] for hardening curve identification—provides a reliable basis for damage model calibration. Furthermore, the integration of these converted trajectories into damage models for the validation of notched and shear geometries mirrors the procedure successfully implemented by Ding et al. [45].

The collective evidence from these studies supports the applicability of Equations 1–4 for the primary alloy characterized in this work. Given that the material exhibits minimal necking prior to fracture, the derived true stress–strain curves provide a robust foundation for GISSMO calibration and accurately capture the deformation mechanics essential for fracture prediction. This methodology is visually corroborated by the post-failure morphology of the smooth tensile specimens, which confirms a restricted necking zone and reinforces the validity of the adopted conversion approach.

The characteristic true stress–true strain response for the investigated specimens is illustrated in Figure 9. From these experimental trajectories, the fracture plastic strain was isolated by partitioning the total strain at failure and removing the elastic component. These derived parameters constitute the foundational input for the GISSMO (Generalized Incremental Stress-State Dependent Damage Model) calibration. Furthermore, these values provide a quantitative measure of the material's multiaxial ductile fracture characteristics across the diverse stress states generated by the varying specimen geometries.

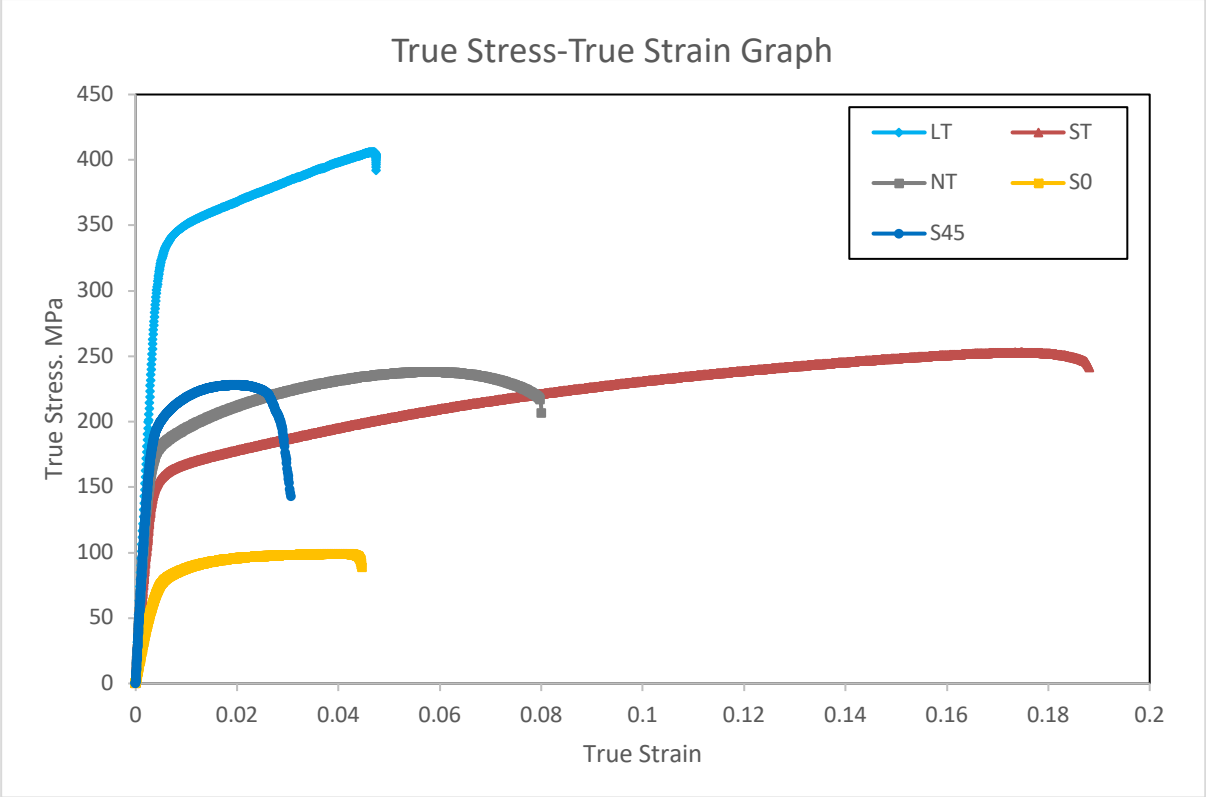

Fig. 9. True Stress-True Strain Graph of Each Specimen

Next, to determine the corresponding stress triaxiality values for each specimen, finite element simulations of the uniaxial tensile tests were performed using Altair HyperWorks, as illustrated in Figure 10. The material properties of the primary aluminium alloy AA6061 employed in the simulations are summarized in Table 2. From these simulations, the stress triaxiality histories and normalized lode angle were plotted against plastic strain curves for each specimen type, as shown in Figure 11. The fracture point was identified based on the experimentally measured fracture plastic strain, and the corresponding stress triaxiality value at the moment of failure was extracted from the simulation results.

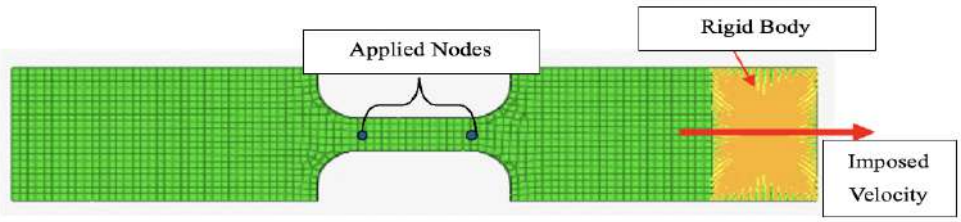

(a) Small Tensile

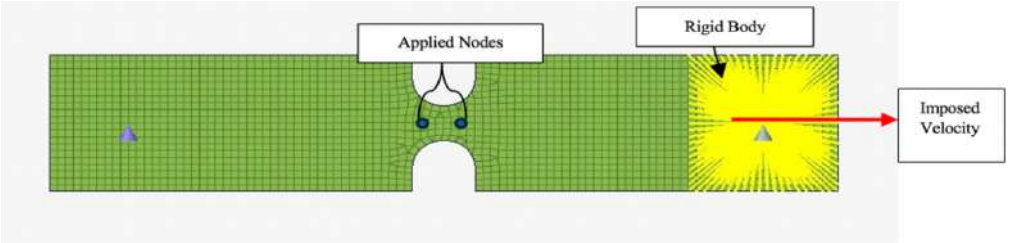

(b) Notched Tensile

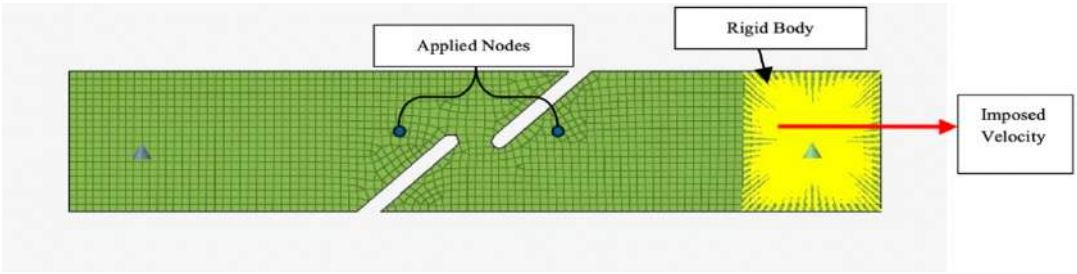

(c) Shear 0°

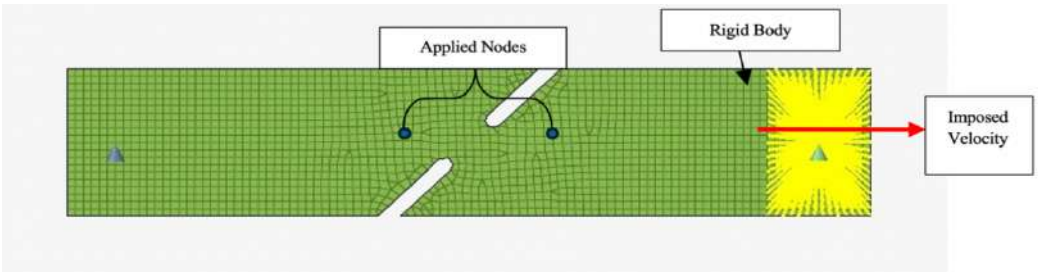

(d) Shear 45°

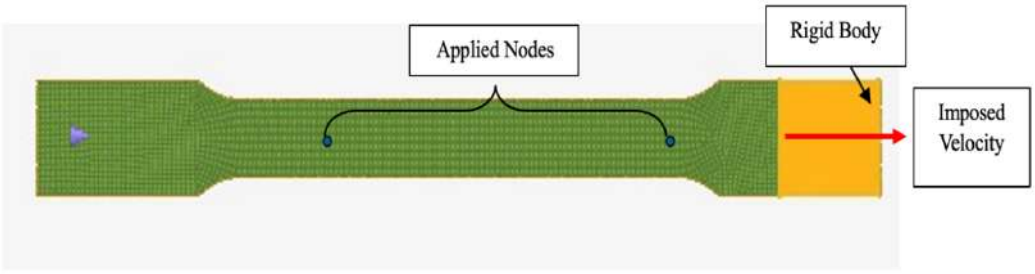

(e) Large Tensile

Fig. 10. Uniaxial Tensile Test Specimen's Simulation in HyperWorks

To characterize the material's failure envelope, the extracted fracture plastic strain values for each geometry were correlated with their corresponding stress triaxiality and normalized Lode angle parameters derived from numerical simulations. This multi-axial dataset was synthesized into a three-dimensional representation, mapping fracture plastic strain against the normalized Lode angle and stress triaxiality and formatted to satisfy the constitutive input requirements of the GISSMO damage model within the HyperWorks environment. These calibrated parameters function as the governing inputs for the failure strain surface, facilitating a high-fidelity representation of the alloy's ductile fracture evolution across diverse loading conditions.

The properties of the primary aluminium alloy AA6061 used in this simulation are presented in Table 3. The plastic hardening behaviour was described using a Simplified Johnson-Cook model, which corresponds to the strain-hardening component of the Johnson–Cook formulation under quasi-static and isothermal conditions, with strain-rate and thermal softening effects intentionally neglected. Equation 5 shows the Simplified Johnson-Cook Model function,

$$\sigma = A + B\varepsilon_p^n \quad \text{(Equation 5)}$$

where *A, B* and *n* values are parameters calibrated from the true stress-true strain graph in the uniform deformation pre-necking region of the tensile test. The engineering stress-engineering strain data were extracted from the plotted force-displacement graph of uniaxial tensile test by using equations 1 and 2. The engineering stress-engineering strain were then converted to true stress-true strain curve by using equations 3 and 4. From the plotted curve, the elastic contribution was removed to obtain the plastic strain value. A least-squares regression was then applied to obtain the Johnson-Cook parameters. The Simplified Johnson-Cook model serves as the constitutive backbone that defines the flow stress before damage initiation. Next, the GISSMO damage model framework is then applied to capture the degradation of this flow stress as a function of plastic strain and triaxiality. This aids in enhancing better results for simulation analysis in predicting the fracture behaviour of primary aluminium alloy.

The obtained hardening function as shown in Table 4 is subsequently applied to all specimen's geometries including notched and shear specimens to plot the stress triaxiality value. This approach is consistent with the theoretical framework of the GISSMO damage model, in which plastic flow is governed by the hardening law, while damage accumulation and fracture are controlled by stress triaxiality-dependent criteria.

It should be noted that the true stress–strain curve used to define the elastoplastic behaviour of primary AA6061 alloy was obtained experimentally at 200 °C and a strain rate of $6\times10^{-}3\ s^{-1}$ [29]. This temperature was selected because it corresponds and relevant to the thermal condition under which the recycled alloy is formed, and it provides a representative softened material response. At this temperature, the strain-rate sensitivity was measurable but not dominant. Since the objective of the present work is to evaluate and improve damage and fracture prediction using GISSMO, the elastoplastic response is intentionally kept consistent by using a single experimentally measured curve. This isolates the effect of the damage model while still providing adequate predictive accuracy.

The numerical simulation results for each specimen geometry were utilized to characterize the evolution of stress triaxiality and the normalized Lode angle relative to plastic strain, as illustrated in Figure 11. The Lode angle parameter is critical for describing the influence of the third invariant of the deviatoric stress tensor, which significantly modifies the fracture strain under shear-dominated loading conditions. The resulting trajectories reflect the expected stress-state transitions for each geometry of small tensile and notched specimens exhibited Lode angle values approaching +1 (axisymmetric tension), while shear specimens yielded values near -1 (axisymmetric compression).

Owing to the limited post-necking deformation characteristic of the primary AA6061 alloy, the fracture response is primarily governed by stress triaxiality. Consequently, the fracture locus established for the GISSMO calibration is formulated as a function of stress triaxiality alone, with the evolution of the normalized Lode angle provided for phenomenological completeness. By correlating the stress triaxiality values at the onset of fracture with the corresponding fracture plastic strain data that were extracted from Figure 9, a robust failure envelope was defined for the subsequent damage modelling workflow.

Table 3
Properties of Primary Aluminium Alloy AA6061 [29]

Elastic Modulus (GPa)	Density ($tonne/mm^3$)	Poisson Ratio	Yield Stress (MPa)
68.9	2.7×10^{-9}	0.33	218

Table 4
Simplified Johnson-Cook Parameter (A, B and n) [29]

Strain rate (/s)	Yield Strength, A (MPa)	Strain Hardening, B (MPa)	Strain Hardening Exponent, n
6×10^{-3}	201.55	250.87	0.206

The compiled data, including fracture plastic strain and corresponding stress triaxiality for each specimen are summarized in Table 5. This dataset serves as a critical input for defining the damage curve in the GISSMO material model and was subsequently implemented in HyperWorks for validation through uniaxial tensile simulations.

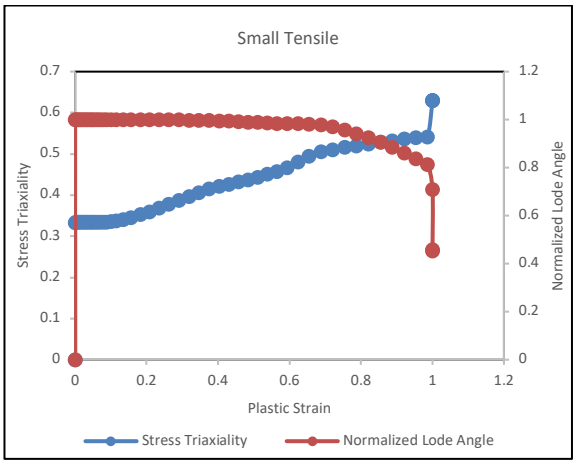

(a)

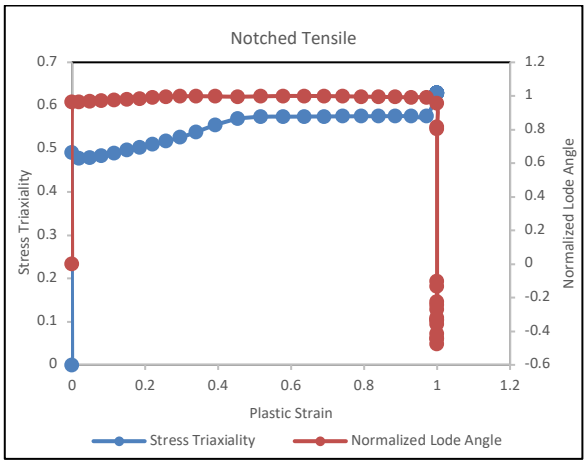

(b)

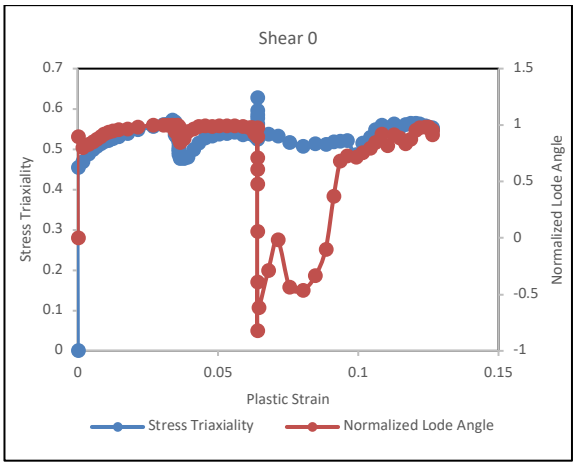

(c)

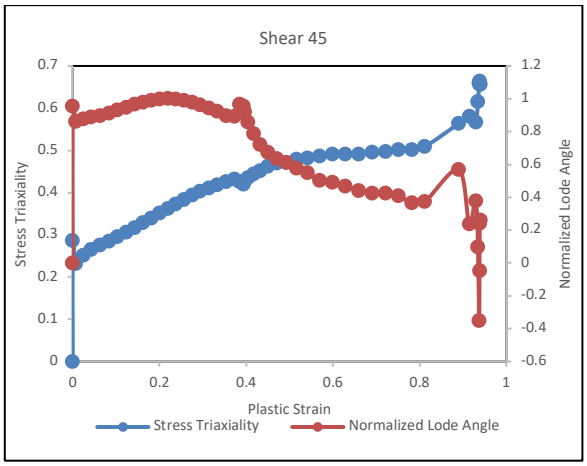

(d)

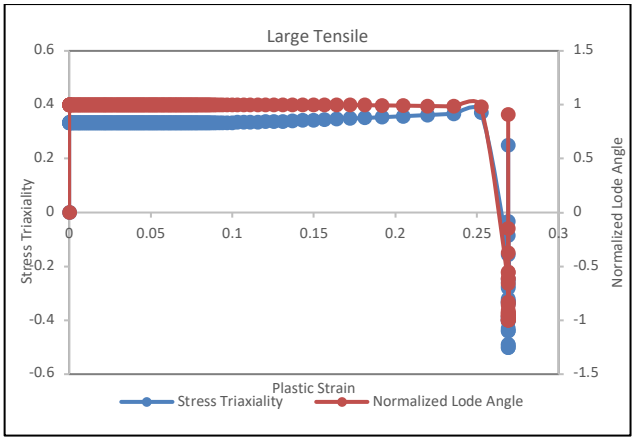

(e)

Fig. 11. Stress triaxiality and Normalized Lode Angle versus Plastic Strain of each Specimen (a) Small Tensile, (b) Notched Tensile, (c) Shear 0°, (d) Shear 45°, (e) Large Tensile

Table 5
Stress Triaxiality and Fracture Plastic Strain for Each Specimen

Specimen	Stress Triaxiality	Fracture Plastic Strain
Small Tensile	0.63	0.18
Notched	0.48	0.075
Shear 0°	-0.43	0.042
Shear 45°	0.45	0.028
Large Tensile	0.33	0.047

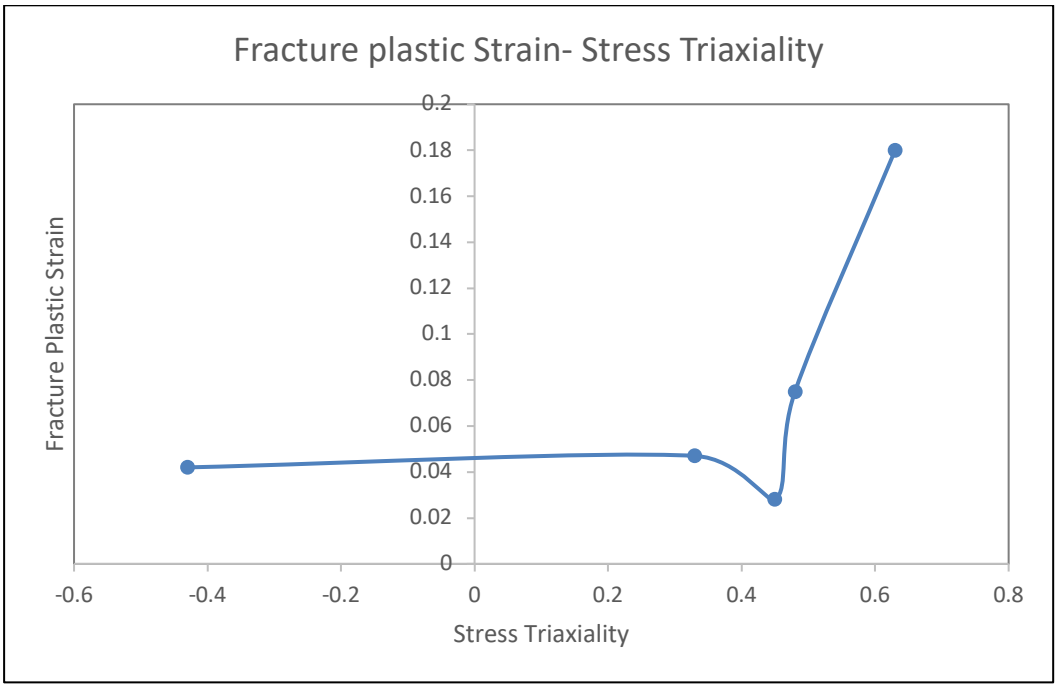

Fig. 12. Fracture Plastic Strain versus Stress Triaxiality Graph

3. Numerical Analysis of GISSMO Damage Model

This section presents the validation of the GISSMO damage model using uniaxial tensile test data. A direct one-to-one comparison was carried out between the experimental and numerical results to evaluate the model's ability to accurately reproduce the material's deformation and fracture behaviour. The comparison of the force–displacement responses demonstrated close agreement in both the elastic region and the onset of yielding, confirming that the calibrated GISSMO model can reliably predict the initial stiffness and yield characteristics of the material before fracture.

The Generalized Incremental Stress-State Dependent Damage Model (GISSMO) is a phenomenological ductile fracture criterion designed to characterize damage evolution and predict fracture initiation. Within the automotive industry, GISSMO is regarded as a premier constitutive framework due to its capacity for high-fidelity simulations of ductile fracture under multiaxial stress states where the capability is essential for crashworthiness and metal-forming analyses [24][30][46][47]. The model concurrently tracks damage accumulation (D) and a localized instability measure (F) through incremental formulations. These measures are functions of the plastic strain ε^P and a damage exponent (n), where the critical strain $\varepsilon_{crit}(\eta)$ and failure strain $\varepsilon_f(\eta)$ are defined as functions of the stress triaxiality, η. The σ_H represent the hydrostatic stress and σ_v represent the equivalent Von Mises stress.

$$\dot{D} = \frac{n}{\wedge(L_e,\eta)\varepsilon_f(\eta)} D^{(1-\frac{1}{n})}\dot{\varepsilon}^p \quad \text{(Equation 6)}$$

$$\dot{F} = \frac{n}{\varepsilon_{crit}(\eta)} F^{(1-\frac{1}{n})}\dot{\varepsilon}^p \quad \text{(Equation 7)}$$

$$\eta = \frac{\sigma_H}{\sigma_V} \quad \text{(Equation 8)}$$

In calibrating GISSMO damage model, the data from the conducted uniaxial tensile tests and simulations were analysed. The stress-strain curve was plotted and extended to true stress-strain curve for each specimen and the value of fracture plastic strain and stress triaxiality were determined. The value of each specimen's fracture plastic strain and stress triaxiality in Table 5 were implemented in HyperWorks and being validated by using uniaxial tensile test simulations. The GISSMO implementation added negligible computational overhead (<5% CPU time) that makes it suitable for large-scale vehicle crash models where the calibration process is data-intensive but computationally efficient once established. This influence by the GISSMO moderate computational overhead due to its damage tracking.

The prediction capability of the GISSMO damage model was validated using uniaxial tensile test data. The simulation results were directly compared with the experimental force–displacement curves to assess the model's accuracy in representing the material behaviour. A one-to-one comparison between the experimental and numerical curves revealed a close agreement, particularly in the elastic region and at the onset of yielding, indicating that the calibrated GISSMO model effectively reproduces the initial deformation response of the material.

3.1 Uniaxial Tensile Test

Before the activation of the GISSMO damage formulation, a purely plastic numerical simulation of the uniaxial tensile test was conducted to independently validate the calibrated hardening behaviour. In this preliminary stage, the damage model was intentionally deactivated to ensure that the predicted numerical response was governed exclusively by the constitutive plasticity law. This decoupling procedure is critical for isolating the hardening calibration from subsequent fracture

modelling, thereby mitigating the risk of misinterpreting softening effects that might otherwise stem from inaccuracies in the plastic parameters. The simulation utilized the identical specimen geometry employed in the preceding stress triaxiality analyses. The material properties of the primary AA6061 alloy were implemented as defined in Table 3, utilizing the specific constitutive parameters detailed in Table 4.

The validity of the numerical framework was established by benchmarking the simulated true stress–strain response against experimental data, with specific emphasis on the elastic modulus, yield strength, and strain-hardening evolution. The assessment prioritized the uniform deformation regime preceding necking to ensure the material response was governed exclusively by plastic flow, independent of damage-induced softening. Key performance indicators utilized for this verification included a comparative analysis of force-displacement trajectories, the identification of necking onset, fracture strain magnitudes, and the morphology of failure localization within the specimen gauge section. By maintaining identical boundary conditions and specimen geometries between the physical tests and the numerical models, the reliability of the hardening calibration and the precision of the damage evolution parameters were systematically verified.

A high degree of correlation at this stage confirms that the calibrated Johnson-Cook hardening parameters (A, B, and n) effectively reproduce the constitutive behaviour of recycled AA6061 under uniaxial loading conditions. The numerical model achieved an average R^2 value of 0.99 across all five geometries which this shows the ability of Johnson-Cook hardening parameters in predicting the material behaviour without any influence from damage model. Furthermore, having an established baseline elastoplastic response through plasticity-only simulations, the following section presents a detailed comparison between the uniaxial tensile experiments and the corresponding numerical predictions. The objective of this comparison is to evaluate the capability of the calibrated constitutive model, including both plasticity and GISSMO damage formulation to accurately reproduce the observed deformation and fracture behaviour.

This sequential validation strategy ensures that subsequent discrepancies in force–displacement curve can be attributed to the damage model rather than inaccuracies in the underlying plasticity formulation. Figure 13 shows the validation curve of force-displacement for plasticity-only simulations. This structured comparison enables a clear distinction between discrepancies arising from plasticity modelling and those associated with damage initiation and fracture evolution. Ultimately, the analysis demonstrates the extent to which the calibrated GISSMO damage model improves the prediction of tensile fracture behaviour for primary AA6061 alloy under quasi-static loading conditions.

Table 6 presents a comparison between the experimentally observed and numerically predicted fracture patterns for all specimen geometries. The simulation results demonstrate a strong correlation with the experimental observations, accurately capturing both the fracture initiation sites and the overall failure morphology. For each specimen type, (small tensile, notched, shear 0°, shear 45°, and large tensile) the predicted fracture locations coincide with those observed in the experimental tests, indicating that the calibrated GISSMO damage model successfully replicates the stress and strain localization behaviour leading to fracture. The high degree of correlation between predicted and physical fracture locations confirms that the GISSMO framework effectively accounts for the complex variations in stress triaxiality. More importantly, the closed agreement at the yield regions across all five geometries proves that a unified calibration framework is capable of capturing the transition from stable plastic flow to damage-induced softening. This confirms that the model is a robust tool for predicting the structural limits of primary AA6061 in high-precision engineering applications.

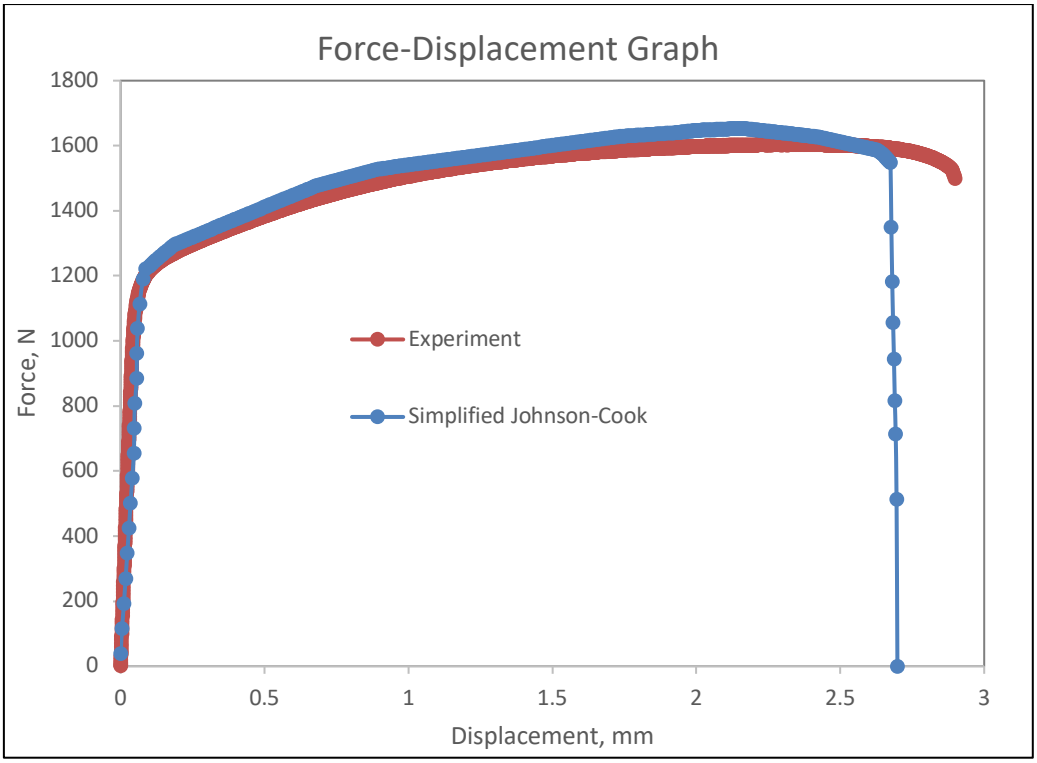

Fig. 13. Plasticity-Only Simulation

Table 6 presents a comparison between the experimentally observed and numerically predicted fracture patterns for all specimen geometries. The simulation results demonstrate a strong correlation with the experimental observations, accurately capturing both the fracture initiation sites and the overall failure morphology. For each specimen type, (small tensile, notched, shear 0°, shear 45°, and large tensile) the predicted fracture locations coincide with those observed in the experimental tests, indicating that the calibrated GISSMO damage model successfully replicates the stress and strain localization behaviour leading to fracture. The high degree of correlation between predicted and physical fracture locations confirms that the GISSMO framework effectively accounts for the complex variations in stress triaxiality. More importantly, the closed agreement at the yield regions across all five geometries proves that a unified calibration framework is capable of capturing the transition from stable plastic flow to damage-induced softening. This confirms that the model is a robust tool for predicting the structural limits of primary AA6061 in high-precision engineering applications.

The accurate prediction of fracture regions across different stress states confirms that the model effectively accounts for variations in different range of stress triaxiality. Furthermore, the similarity in crack propagation paths and failure modes highlights the robustness of the GISSMO calibration in describing damage evolution under both tensile and shear-dominated loading conditions. Overall, the close agreement between the simulated and experimental fracture morphologies provides strong validation that the developed GISSMO model can reliably predict material failure mechanisms in primary AA6061 aluminium alloy.

Table 6
Comparison of Simulation and Experiment Fractured Specimens

Types of specimens	Simulation Results	Experiment Results
Small Tensile	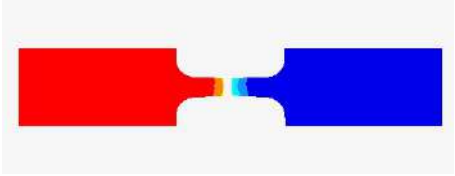	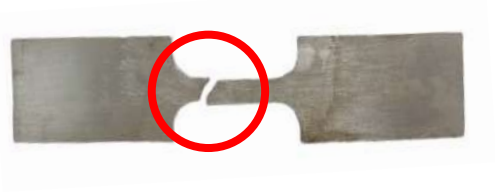
Notched Tensile	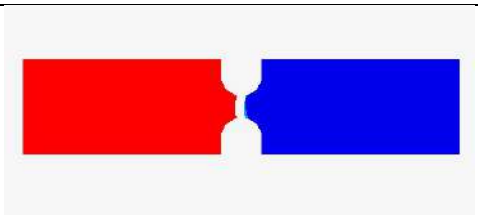	
Shear 0°	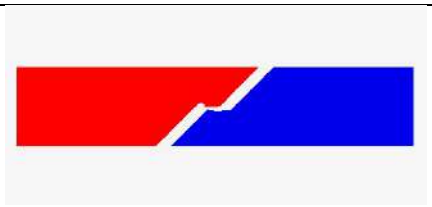	
Shear 45°	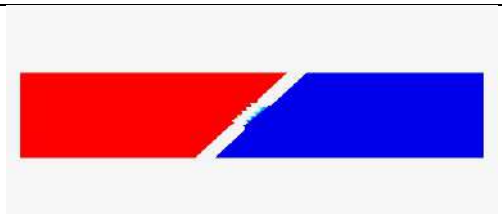	
Large tensile	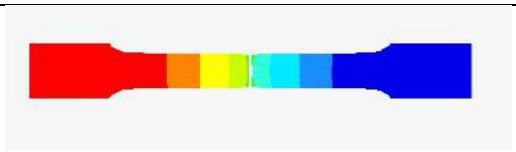	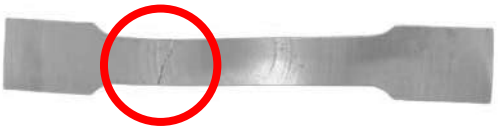

The comparison of the force–displacement responses between the experimental and simulation results for all specimen geometries demonstrates excellent overall agreement. The elastic region and yield onset are well captured across all specimens, confirming that the calibrated GISSMO damage model accurately reproduces the initial stiffness and yielding behaviour of the primary AA6061 alloy. For the small and large tensile specimens, the simulated curves closely follow the experimental trends throughout the deformation process, similarly for notched and shear specimens which exhibit strong correlation in both the peak load and fracture displacement.

As shown in table 7, the inclusion of shear geometries demonstrated that AA6061 yields earlier and exhibits its lowest strength and ductility under shear-dominated loading. Specifically, the comparison between Shear 0° and Shear 45° reveals that mixed loading modes (shear and tension) significantly enhance the load-bearing area and strength. This insight is vital for automotive

designers, as it proves that standard tensile data alone cannot accurately predict failure in real-world crash scenarios where shear-localised deformation is the dominant failure mechanism.

These results indicate that the GISSMO parameters can represent the material response under various stress states, ranging from uniaxial to shear-dominated conditions. Furthermore, the predicted softening behaviour and the onset of fracture align well with the experimental observations, demonstrating that the model effectively captures both the damage initiation and progressive degradation until failure. Overall, the close correspondence between the experimental and numerical curves validates the accuracy and robustness of the calibrated GISSMO model in predicting the deformation and fracture behaviour of the aluminium alloy AA6061 under complex loading conditions.

Table 7
Comparison of Experiment and Simulation Force-Displacement Graph

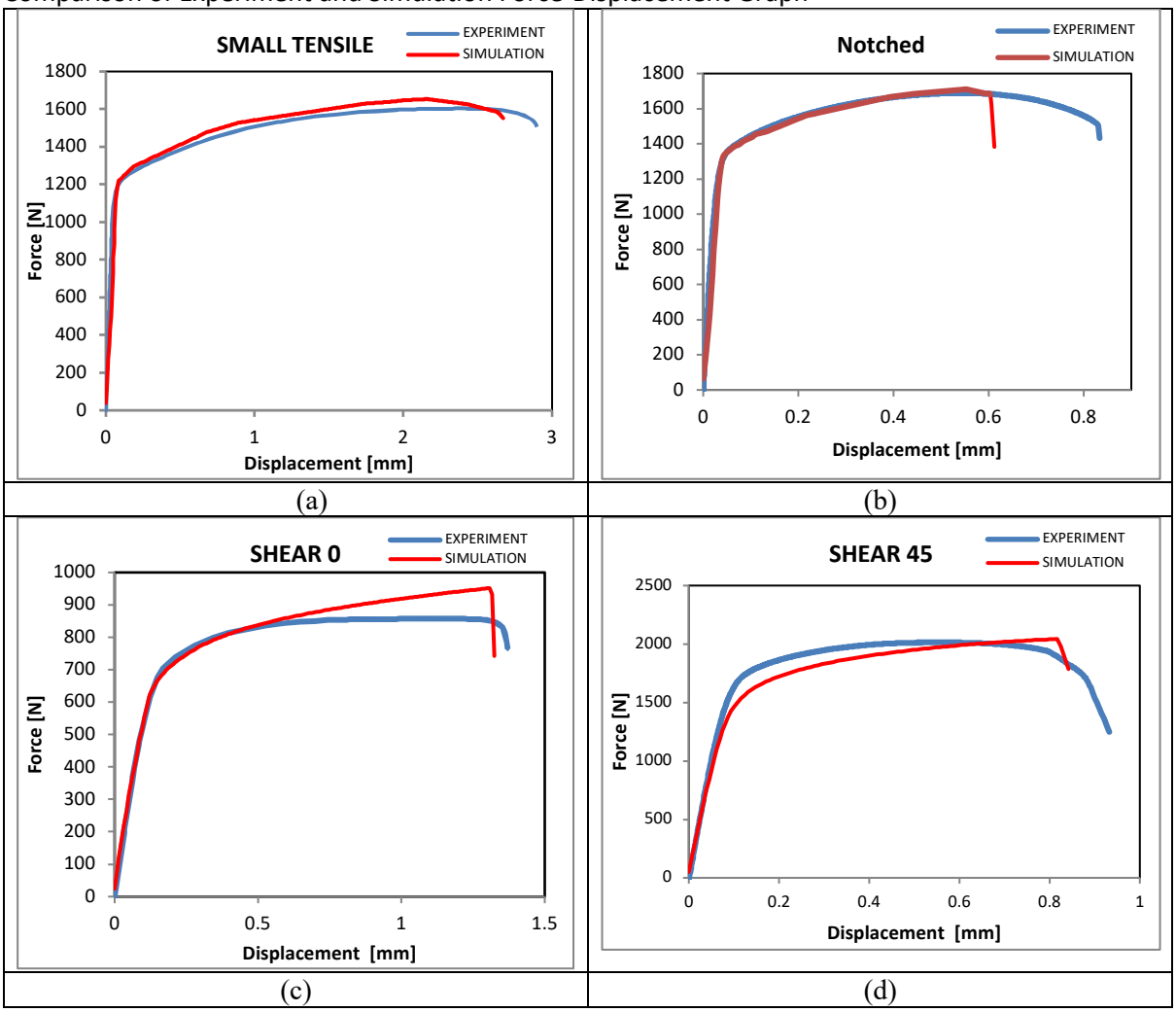

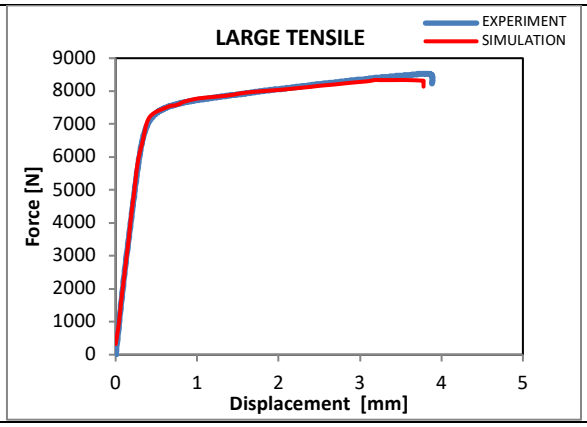

(e)

Moreover, to verify quasi-static consistency prior to damage calibration, stress uniformity within the critical deformation regions of all specimen configurations was evaluated before the onset of necking or localisation. For each specimen type (small tensile, notched tensile, large tensile and shear), the time histories of stress and strain were extracted from selected integration points within the gauge or shear zone. The spatial distribution of these variables was examined to confirm stable force or load transfer and absence of numerical oscillations. This procedure was conducted prior to activating the GISSMO damage formulation to ensure that the deformation response was governed solely by the calibrated plasticity model. The selected elements for each specimen were chosen from the applied nodes area as shown in Figure 10.

Figures 14 and 15 illustrate the temporal evolution of stress and strain, respectively, extracted from discrete integration nodes situated along the specimen gauge section. The stress histories at these nodal locations exhibit a distinct spatial gradient across the gauge length, with Node 1 maintaining higher magnitudes than Node 2 due to its proximity to the applied loading boundary. This variation effectively characterizes the non-uniform stress distribution inherent within the gauge area during uniaxial extension. An analogous trend is observed in the strain-time histories, confirming a consistent spatial decay in deformation magnitude across the region of interest. Notably, the smooth and monotonic evolution of both stress and strain signals, devoid of spurious oscillations or numerical artifacts demonstrates the constitutive framework provides a stable and physically consistent prediction of the material response.

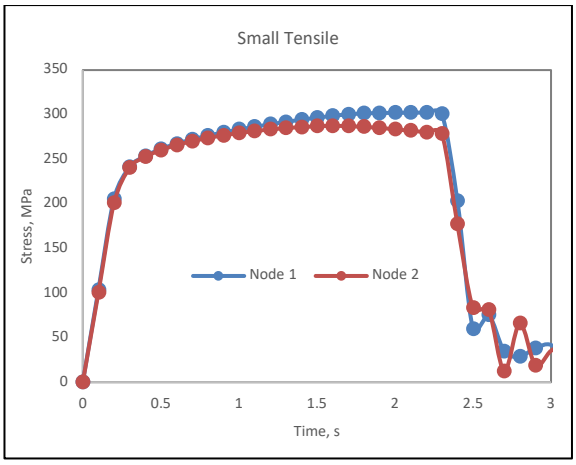

(a)

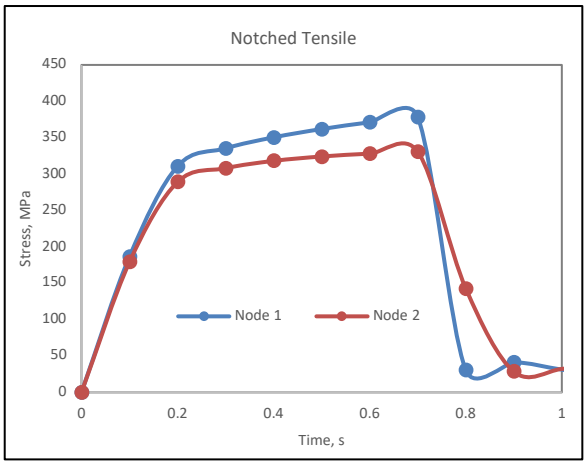

(b)

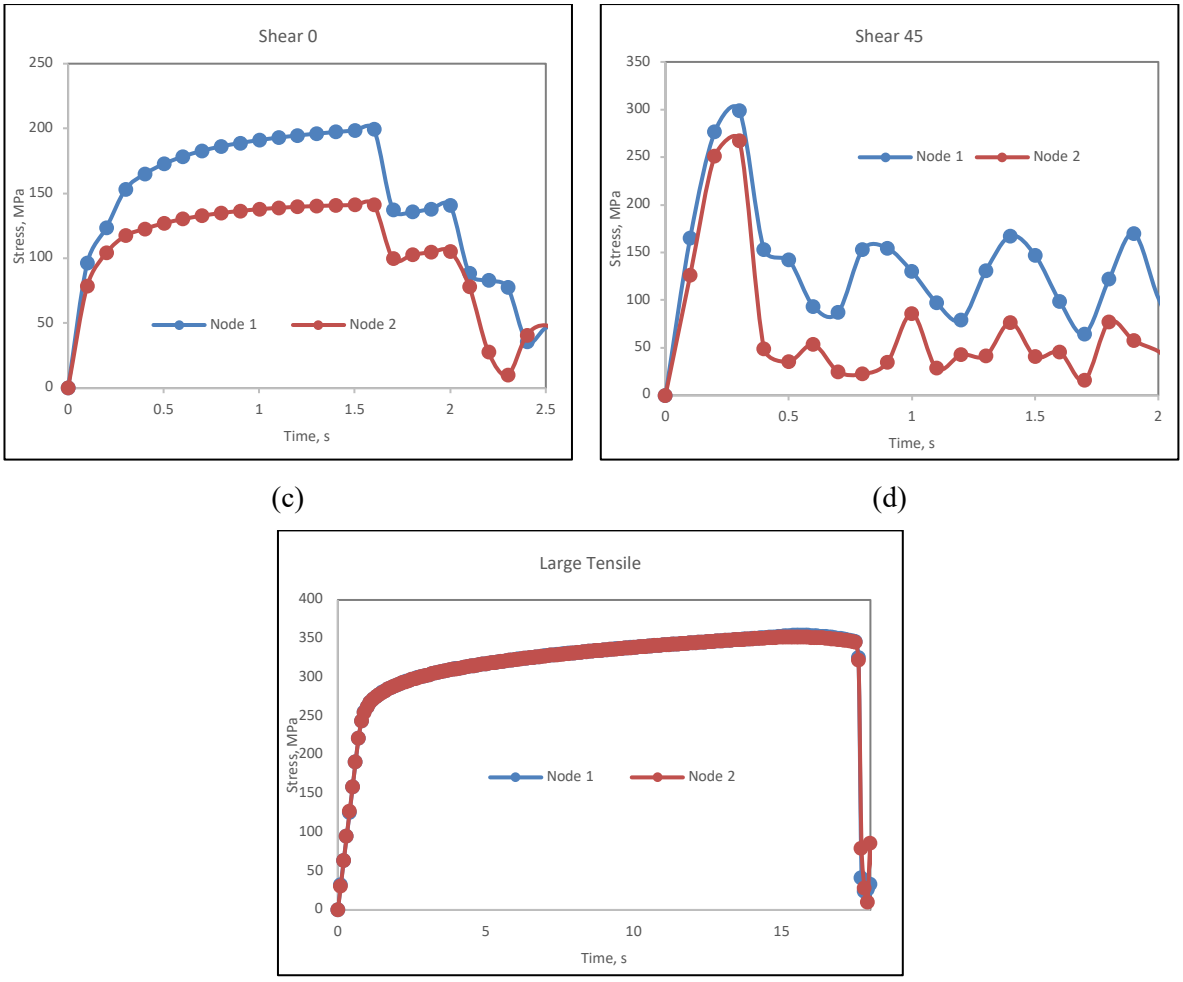

Fig. 14. Time Histories Graph of Stress-Time (a) Small Tensile, (b) Notched Tensile, (c) Shear 0, (d) Shear 45, (e) Large Tensile

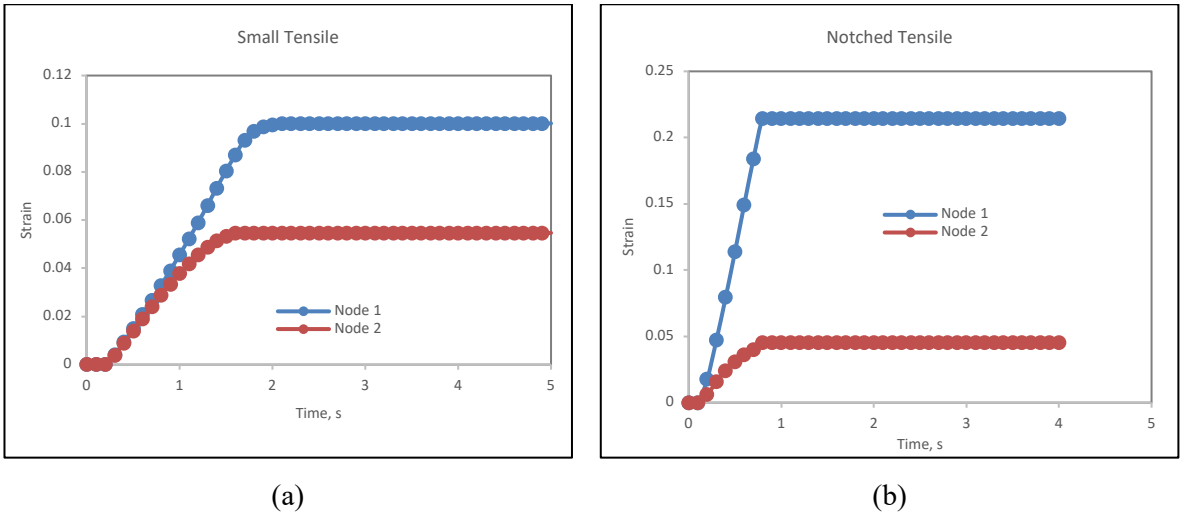

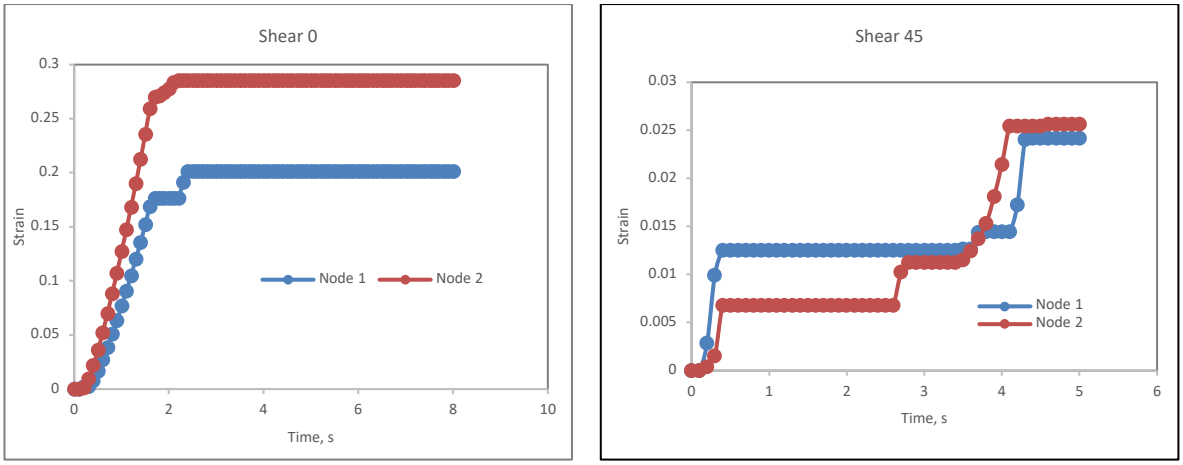

(c)

(d)

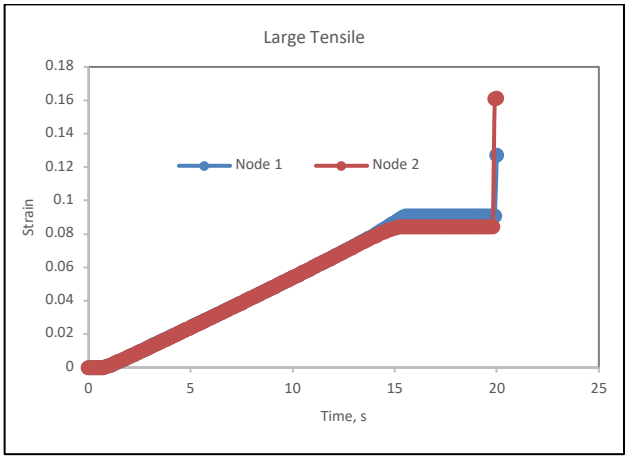

(e)

Fig. 15. Time Histories Graph of Strain-Time (a) Small Tensile, (b) Notched Tensile, (c) Shear 0, (d) Shear 45, (e) Large Tensile

3.2 Model Limitations

While the developed GISSMO framework provides a high-fidelity fracture prediction for primary AA6061, several inherent limitations and physical assumptions must be acknowledged to ensure the proper application of these results. A primary concern in finite element damage modelling is mesh dependency. The current model utilized a consistent mesh size of 1mm for all specimen geometries to maintain calibration integrity. However, local fracture strain values in GISSMO are sensitive to element size. Therefore, applying these parameters to larger structural components, such as automotive bumper beams, would necessitate characteristic length scaling or regularization to prevent premature failure predictions in coarser meshes.

Furthermore, the loading conditions in this study were restricted to the quasi-static regime, with experimental data acquired at a strain rate of $6\times10^{-}3\ s^{-1}$. While this rate is a standard baseline for material characterization, it does not explicitly account for the high strain-rate sensitivity or adiabatic heating effects prevalent in actual vehicle crash events. Similarly, the constitutive behaviour defined by the Simplified Johnson-Cook model in this work was benchmarked against data obtained at 200 °C. In real-world applications, performance may vary across a broader thermal spectrum, suggesting

that future iterations of the model could benefit from incorporating a more comprehensive range of temperature and rate-dependent experimental data.

Additionally, material variability and microstructural assumptions present a source of potential uncertainty. As a precipitation-hardened Al-Mg-Si alloy, the failure envelope of AA6061 can be influenced by minor batch-to-batch variations in microstructural precipitates. The current formulation assumes material isotropy, however, manufacturing processes such as extrusion can introduce directional dependencies that were not explicitly captured in this study. These factors, alongside the "measurement artifacts" observed in small tensile specimens due to machine compliance, highlight that while the model shows a high degree of correlation with experimental results, it remains a numerical approximation of complex physical phenomena. Acknowledging these limitations ensures a more scientific and transparent framework for high-precision engineering applications.

4. Conclusion

This study established a high-fidelity fracture prediction framework for AA6061 primary aluminium alloy by successfully developing and validating the Generalized Incremental Stress-State Dependent Damage Model (GISSMO) through a hybrid experimental-numerical approach. By subjecting five distinct specimen geometries (small tensile, large tensile, notched tensile, shear 0°, and shear 45°) to uniaxial loading, the research captured a wide spectrum of stress states representative of real-world automotive crash conditions. The experimental results revealed significant variations in fracture response across these geometries, highlighting the profound influence of stress triaxiality and constraint on the material's ductile behaviour. As proven in the study, AA6061 exhibits high ductility in smooth tensile states with reduction of fracture strain value under high-triaxiality notched conditions, demonstrating a critical sensitivity that must be accounted for in designing the bumper beam designs. The calibrated GISSMO parameters accurately characterized progressive damage initiation and fracture evolution, providing a complete fracture envelope for the alloy. This allows automotive engineers to reduce safety factors and material thickness in aluminium-intensive designs without compromising crash safety.

Numerical validation conducted via Finite Element Analysis (FEA) demonstrated an excellent correlation between experimental force-displacement curves and simulation results, confirming the model’s superior predictive capability. Furthermore, the spatial consistency between the physical rupture zones and the simulated fracture areas validates the accuracy of the damage localization parameters. To ensure the scientific integrity of the framework, a plasticity-only baseline analysis was performed to isolate the constitutive response. This confirmed that while plastic flow governs the fundamental load-deformation response, the integration of damage modelling is essential for capturing localized failure. This was further substantiated by internal stress and strain time-history analyses at the gauge area, which revealed physically consistent deformation localization and load redistribution.

The implementation of the validated GISSMO framework for AA6061 marks a significant transition from conservative "trial-and-error" methodologies to high-fidelity predictive engineering in automotive design. By accurately capturing the transition between shear and tensile failure modes under multi-axial loading, this model enables designers to optimize the cross-sectional geometry and wall thickness of crash-relevant extrusions, such as bumper beams and longitudinal members. This precision facilitates substantial material weight reduction, enhancing fuel efficiency or battery range while ensuring superior crash energy management by accurately predicting the performance of crush initiators. Ultimately, providing a robust fracture envelope that correlates closely with experimental

data reduces the reliance on expensive physical prototyping and ensures that structural components are engineered to reach their full energy-absorption potential without premature failure, thereby elevating the safety standards of modern vehicle architectures.

Acknowledgement
This research was supported by Universiti Tun Hussein Onn Malaysia through TIER 1 Research Grant Scheme, Vot Q897.

References

[1] W. Zhang and J. Xu, "Advanced lightweight materials for Automobiles: A review," Sep. 01, 2022, *Elsevier Ltd*. doi: 10.1016/j.matdes.2022.110994.
[2] B. Du, Q. Li, C. Zheng, S. Wang, C. Gao, and L. Chen, "Application of Lightweight Structure in Automobile Bumper Beam: A Review," Feb. 01, 2023, *MDPI*. doi: 10.3390/ma16030967.
[3] M. Tisza and I. Czinege, "Comparative study of the application of steels and aluminium in lightweight production of automotive parts," *International Journal of Lightweight Materials and Manufacture*, vol. 1, no. 4, pp. 229–238, Dec. 2018, doi: 10.1016/j.ijlmm.2018.09.001.
[4] P. Mukhopadhyay, "Alloy Designation, Processing, and Use of AA6XXX Series Aluminium Alloys," *ISRN Metallurgy*, vol. 2012, pp. 1–15, Apr. 2012, doi: 10.5402/2012/165082.
[5] W. S. Miller *et al.*, "Recent development in aluminium alloys for the automotive industry," 2000. [Online]. Available: www.elsevier.com/locate/msea
[6] Team Xometry, "Aluminium: History, Characteristics, Types, Properties and Applications," Mar. 2023, Accessed: Apr. 29, 2024. [Online]. Available: https://www.xometry.com/resources/materials/what-is-aluminum/
[7] O. Daghfas, A. Znaidi, A. Ben Mohamed, and R. Nasri, "Experimental and numerical study on mechanical properties of aluminum alloy under uniaxial tensile test," *Frattura ed Integrita Strutturale*, vol. 11, no. 39, pp. 263–273, Jan. 2017, doi: 10.3221/IGF-ESIS.39.24.
[8] C. Gui, J. Bai, and W. Zuo, "Simplified crashworthiness method of automotive frame for conceptual design," *Thin-Walled Structures*, vol. 131, pp. 324–335, 2018, doi: https://doi.org/10.1016/j.tws.2018.07.005.
[9] C. K. P. R. M. M. R. Reichert, "Development of Integrated Vehicle-Occupant Model for Crashworthiness Safety Analysis," Dec. 2014.
[10] J. Marzbanrad, S. Noruzi, and A. Ahmadi, "Damage modeling in crashworthiness of dual-phase steel," 2013.
[11] M. W. D. M. H. & Y. I. Baccouche, "Crashworthiness Challenges in Steel-to-Aluminum Front End Design," *Proceedings of the ASME 2002 International Mechanical Engineering Congress and Exposition. Transportation: Making Tracks for Tomorrow's Transportation*, pp. 169–182, Nov. 2002, Accessed: Apr. 09, 2025. [Online]. Available: https://doi.org/10.1115/IMECE2002-39076
[12] International Aluminium Institute. (2020). Aluminium Recycling: A Pathway to Sustainability. https://international-aluminium.org
[13] Vignjevic, R., Bourne, N. K., Millett, J. C. F. and De Vuyst, T. (2002), "Effects of orientation on the strength of the aluminium alloy 7010-T6 during shock loading: Experiment and simulation", Journal of Applied Physics, vol. 92, no. 8, pp. 4342-4348
[14] Gray, G.T., Bourne, N.K., Millett, J.C.F., (2003), "Shock response of tantalum: lateral stress and shear strength through the front", Journal of Applied Physics 94(10), 6430–6436.
[15] Khan, A. S., Kazmi, R. and Farrokh, B. (2007a), "Multiaxial and non-proportional loading responses, anisotropy and modeling of Ti–6Al–4V titanium alloy over wide ranges of strain-rates and temperatures", International Journal of Plasticity, vol. 23, no. 6, pp. 931-950
[16] Khan, A. S., Kazmi, R., Farrokh, B. and Zupan, M. (2007b), "Effect of oxygen content and microstructure on the thermo-mechanical response of three Ti–6Al–4V alloys: Experiments and modeling over a wide range of strain-rates and temperatures", International Journal of Plasticity, vol. 23, no. 7, pp. 1105-1125
[17] Nakamachi, E., Tam, N. N. and Morimoto, H. (2007), "Multi-scale finite element analyses of sheet metals by using SEM-EBSD measured crystallographic RVE models", International Journal of Plasticity, vol. 23, no. 3, pp. 450-489
[18] Khan, A. S., Kazmi, R., Pandey, A. and Stoughton, T. (2009), "Evolution of subsequent yield surfaces and elastic constants with finite plastic deformation. Part-I: A very low work hardening aluminium alloy (Al6061-T6511)", *International Journal of Plasticity*, vol. 25, no. 9, pp. 1611-1625
[19] Sitko, M., Skoczeń, B. and Wróblewski, A. (2010), "FCC-BCC phase transformation in rectangular beams subjected to plastic straining at cryogenic temperatures", *International Journal of Mechanical Sciences,* vol. 52, no. 7, pp. 993-1007

[20] Mohd Nor, M.K., Ma'at, N. & Ho, C.S. An anisotropic elastoplastic constitutive formulation generalised for orthotropic materials. Continuum Mech. Thermodyn. 30, 825–860 (2018). https://doi.org/10.1007/s00161-018-0645-7

[21] A. M. Elmarakbi, N. Hu, and H. Fukunaga, "Finite element simulation of delamination growth in composite materials using LS-DYNA," *Compos. Sci. Technol.*, vol. 69, no. 14, pp. 2383–2391, Nov. 2009, doi: 10.1016/J.COMPSCITECH.2009.01.036.

[22] M. K. Mohd Nor, C. S. Ho, N. Ma'at, and M. F. Kamarulzaman, "Modelling shock waves in composite materials using generalised orthotropic pressure," *Contin. Mech. Thermodyn.*, vol. 32, no. 4, pp. 1217–1229, Jul. 2020, Accessed: May 02, 2021. [Online]. Available: https://link.springer.com/article/10.1007/s00161-019-00835-6

[23] T. Wierzbicki and Y. Bao, "Calibration and evaluation of seven fracture models," Int. J. Mech. Sci., vol. 47, no. 4–5, pp. 719–743, 2005.

[24] R. Borsari, G. Belingardi, and M. P. Cavatorta, "Application of the GISSMO model for predicting ductile fracture in crash simulations," Eng. Fract. Mech., vol. 200, pp. 22–34, 2018

[25] Neukamm, F., Feucht, M., & Haufe, A. (2009). *Considering damage history in crashworthiness simulations*.

[26] Otroshi, M., Rossel, M., & Meschut, G. (2020). Stress state dependent damage modeling of self-pierce riveting process simulation using GISSMO damage model. *Journal of Advanced Joining Processes*, *1*. https://doi.org/10.1016/j.jajp.2020.100015

[27] Borsari, R., Belingardi, G., & Cavatorta, M. P. (2018). Application of the GISSMO model for predicting ductile fracture in crash simulations. Engineering Fracture Mechanics, 200, 22–34. https://doi.org/10.1016/j.engfracmech.2018.07.014

[28] Andrade, F., & Feucht, M. (2017a). *A comparison of damage and failure models for the failure prediction of dual-phase steels*.

[29] Ma, N., Khir Mohd Nor, M., Sin Ho, C., Abdul Latif, N., Emran Ismail, A., Kamarudin, K.-A., Jamian, S., Norihan Ibrahim, M., & Khairudin Awang, M. (2019). Effects of Temperatures and Strain Rate on the Mechanical Behaviour of Commercial Aluminium Alloy AA6061. *Journal of Advanced Research in Fluid Mechanics and Thermal Sciences Journal Homepage*, *54*, 21–26. www.akademiabaru.com/arfmts.html

[30] Andrade, A., Alves, M., & Andrade-Campos, A. (2016). A Generalized Incremental Stress-State Dependent Damage Model. International Journal of Fracture, 199, 165–187. https://link.springer.com/article/10.1007/s10704-016-0081-2

[31] S. Moakhar, H. Hentati, M. Barkallah, J. Louati, and M. Haddar, "Influence of geometry on stress state in bulk characterization tests," *Comptes Rendus - Mecanique*, vol. 347, no. 12, pp. 930–943, Dec. 2019, doi: 10.1016/j.crme.2019.10.003.

[32] M. Dunand, "Ductile fracture at intermediate stress triaxialities: Experimental investigations and micro-mechanical modeling," 2008.

[33] M. F. Alam, V. Balaji, F. Tucci, H. Krishnaswamy, and U. Chakkingal, "A critical evaluation of shear specimen geometry for accurate stress triaxiality control," *Eng Fract Mech*, vol. 328, p. 111562, 2025, doi: https://doi.org/10.1016/j.engfracmech.2025.111562.

[34] Wang, L., Park, J. H., & Choi, N. S. (2020). Observation of notch effect in Al6061-T6 specimens under tensile loading using digital image correlation and finite element method. Journal of Mechanical Science & Technology, 34(3), 1049–1058. https://doi.org/10.1007/s12206-020-0207-3
DOI: 10.1007/s12206-020-0207-3

[35] L. Y. Kou, W. Y. Zhao, X. Y. Tuo, G. Wang, and C. R. Sun, "Effect of stress triaxiality on fracture failure of 6061 aluminium alloy," *Journal of Mechanical Engineering and Sciences*, vol. 14, no. 2, pp. 6961–6970, Jun. 2020, doi: 10.15282/JMES.14.2.2020.33.0545.

[36] Li, Y., Liu, Y., & Sun, Q. (2019). Influence of notch radius on tensile behavior and ductile fracture of aluminum alloy AA6061. Engineering Fracture Mechanics, 216, 106505.

[37] Mishra, A., Kim, J. Y., & Meyers, M. A. (2005). Scale effects and influence of specimen size on tensile properties of metallic alloys. Materials Science and Engineering A, 410–411, 289–291.

[38] Harwell, J., Balanethiram, A., & Prakash, V. (2025). Experimental quantification of geometry and stress-state effects on failure limits of Al-6061 using notched and shear specimens. Journal of Materials Processing Technology, 324, 117012.

[39] Ding, J., Bao, K., Zhu, X., Tian, X., & Li, X. (2022). Effects of stress state and strain rate on the deformation and fracture mechanisms of AA6061 aluminum alloy. Materials Science and Engineering A, 847, 143488.

[40] Hong, S., Zhang, H., Li, Y., Jin, C., & Shi, H. (2023). Fracture behavior of aluminum alloy 6061 under different stress states: Comparison between shear and tensile loading. International Journal of Mechanical Sciences, 241, 108000.

[41] I. A. F. Latif, M. K. M. Nor, N. K. Yusuf, S. K. Subramaniyan, M. S. A. Samad, and N. Ma'at, "Quantitative Characterization of the Perforation Behaviour of Direct Recycled aluminium Alloy 6061 Plates Subjected to High-

Velocity Impact," *Journal of Advanced Research in Applied Mechanics*, vol. 118, no. 1, pp. 193–211, Jun. 2024, doi: 10.37934/aram.118.1.193211.

[42] Hyun, H. C., Kim, M., Bang, S., & Lee, H. (2014). On acquiring true stress-strain curves for sheet specimens using tensile test and FE analysis based on a local necking criterion. *Journal of Materials Research*, *29*(5), 695–707. https://doi.org/10.1557/jmr.2014.24

[43] Koch, D., Andrade, F., & Haufe, A. (2022). 07_gissmo. *Material Competence Center DYNAmore*.

[44] Chen, X., Chen, G., Huang, L., & Shi, M. F. (2018). *5 th International LS-DYNA ® Users Conference Calibration of GISSMO Model for Fracture Prediction of A Super High Formable Advanced High Strength Steel*.

[45] Ding, F., Hong, T., Xu, Y., & Jia, X. (2022). Prediction of Fracture Behavior of 6061 Aluminum Alloy Based on GTN Model. *Materials*, *15*(9). https://doi.org/10.3390/ma15093212

[46] J. Zhang, X. Zhou, and L. Wang, "Validation of ductile fracture models using drop-weight impact testsing of aluminium extrusions," Int. J. Impact Eng., vol. 154, pp. 103882, 2021.

[47] Chen, C., Lee, Y., Sun, X., & Liu, W. (2018). GISSMO Model Validation for 980GEN3 AHSS in Crash Simulation. SAE Technical Paper 2018-01-0107. https://www.sae.org/publications/technical-papers/content/2018-01-0107/